Journal of Controlled Release 348 (2022) 1004–1015

Contents lists available at ScienceDirect

Journal of Controlled Release

journal homepage: www.elsevier.com/locate/jconrel

Spatial specific delivery of combinational chemotherapeutics to combat intratumoral heterogeneity

Kewei Wang [a,b,1], Maolin Jiang [a,b,1], Jielian Zhou [a,c], Yansong Dong [a,d], Ye Liu [a,d], Qingyu Zong [a,d], Puja Sandbhor [e], N.D. Pradeep Singh [f], Youyong Yuan [a,b,*]

[a] School of Biomedical Sciences and Engineering, South China University of Technology, Guangzhou International Campus, Guangzhou 511442, PR China
[b] National Engineering Research Center for Tissue Restoration and Reconstruction, South China University of Technology, Guangzhou 510006, PR China
[c] Guangdong Provincial Key Laboratory of Biomedical Engineering, South China University of Technology, Guangzhou 510006, PR China
[d] Key Laboratory of Biomedical Materials and Engineering of the Ministry of Education, South China University of Technology, Guangzhou 510006, PR China
[e] Department of Biosciences and Bioengineering, Indian Institute of Technology Bombay, Powai, 400076, India
[f] Department of Chemistry, Indian Institute of Technology Kharagpur, Kharagpur 721302, India

ARTICLE INFO

Keywords:
Bioorthogonal chemistry
Size transformable nanocarrier
Intratumoral heterogeneity
Combination chemotherapy
Tumor hypoxia

ABSTRACT

Hypoxia-induced intratumoral heterogeneity poses a major challenge in tumor therapy due to the varying susceptibility to chemotherapy. Moreover, the spatial distribution patterns of hypoxic and normoxic tissues makes conventional combination therapy less effective. In this study, a tumor-acidity and bioorthogonal chemistry mediated in situ size transformable nanocarrier (NP@DOX_{DBCO} plus $iCPPA_{N3}$) was developed to spatially deliver two combinational chemotherapeutic drugs (doxorubicin (DOX) and PR104A) to combat hypoxia-induced intratumoral heterogeneity. DOX is highly toxic to tumor cells in normoxia state but less toxic in hypoxia state due to the hypoxia-induced chemoresistance. Meanwhile, PR104A is a hypoxia-activated prodrug has less toxic in normoxia state. Two nanocarriers, NP@DOX_{DBCO} and $iCPPA_{N3}$, can cross-link near the blood vessel extravasation sites through tumor acidity responsive bioorthogonal click chemistry to enhance the retention of DOX in tumor normoxia. Moreover, PR104A conjugated to the small-sized dendritic polyamidoamine (PAMAM) released under tumor acidity can penetrate deep tumor tissues for hypoxic tumor cell killing. Our study has demonstrated that this site-specific combination chemotherapy is better than the traditional combination chemotherapy. Therefore, spatial specific delivery of combinational therapeutics via in situ size transformable nanocarrier addresses the challenges of hypoxia induced intratumoral heterogeneity and provides insights into the combination therapy.

1. Introduction

Tumor has a high level of heterogeneity in the cellular and molecular signatures within a lesion, as results of tumor cells constantly change genome and protein expression to adapt to its microenvironment [1–5]. Tumor heterogeneity is a major challenge in chemotherapy due to the different susceptibility of cells to chemotherapeutics within a solid tumor [6–8]. For instance, hypoxia is in most tumors due to the imbalance between oxygen demand and supply [9–11]. The tumor cell oxygen levels decrease as the distance from the blood vessel increases, and the uneven oxygen distribution in tumor tissues causes intratumoral heterogeneity, leading to insufficient therapeutic benefit [12–17]. Hypoxic tumor cells are less sensitive to radiotherapy, photodynamic therapy, chemotherapy, and immunotherapy than normoxic tumor cells [18–21]. Hypoxia promotes resistance to chemotherapy by up-regulating the levels of P-glycoprotein (P-gp), thus enhancing drug efflux and leading to treatment failure [22,23]. Although some chemotherapeutics, including doxorubicin (DOX), cisplatin, and sorafenib are widely used, they are less effective in hypoxic microenvironment, especially where pO_2 is lower than 2.5 mmHg [24–26]. In contrast, hypoxia-activated prodrugs (HAPs) have higher cytotoxicity in hypoxic cells than in normoxic cells due to the difference in redox [17,27,28].

* Corresponding author at: School of Biomedical Sciences and Engineering, South China University of Technology, Guangzhou International Campus, Guangzhou 511442, PR China.
E-mail address: yuanyy@scut.edu.cn (Y. Yuan).
[1] Contributed equally to this work.

https://doi.org/10.1016/j.jconrel.2022.06.046
Received 12 March 2022; Received in revised form 16 June 2022; Accepted 25 June 2022
Available online 2 July 2022

Therefore, HAPs can selectively kill hypoxic tumor cells, thus converting tumor hypoxia from a problem to a selective treatment advantage [29]. Considering the spatial distribution patterns of hypoxic and normoxic tissues, on-demand spatial delivery of appropriate drugs to designated tumor cells is a promising strategy for overcome hypoxia-induced intratumoral heterogeneity.

A strategy that can spatial-specific deliver combinational therapeutics into corresponding tumor cells is crucial for site-specific and selective chemotherapy [30–32]. Nanoparticles are excellent for drug delivery and can simultaneously load multiple therapeutic agents [33,34]. However, most reported nanomedicines have been designed to co-deliver therapeutic agents into one tumor cell, and they do not efficiently accumulate in hypoxic tumor regions due to the spatially disorganized tumor vasculature and dense extracellular matrix [35–37]. Therefore, new strategies are needed to overcome the biological barriers for efficient spatial specific delivery of combinational therapeutics to improve the therapeutic effect of nanomedicine [38,39]. Size is one of the most important characteristics of nanoparticles, which has multiple effects on the nanomedicine in the body, including circulation, biodistribution, accumulation, retention, penetration and internalization, and can further affect the therapeutic effect of nanoparticles [35,40]. Small-sized nanoparticles have enhanced penetration with limited accumulation at the tumor site, while large-sized nanoparticles have improved tumor accumulation with poor tumor tissue penetration [35,41–43]. Therefore, size also regulates the distribution of nanotherapeautics in tumor tissues. Large-sized nanomedicines can only be enriched in the surface area near the tumor blood vessel due to limited penetration, while small-sized nanoparticles can penetrate into deep tumor tissues due to excellent tumor penetration properties [40]. Therefore, spatial targeted delivery into different depths of the tumor tissue can be achieved by modulating the size of nanoparticles in the tumor situ.

Herein, a *in situ* size transformable nanocarrier (NP@DOX_{DBCO} plus $iCPPA_{N3}$) was developed to spatially deliver DOX and hypoxia-activated prodrug PR104A to normoxic and hypoxic tumor cells for combating hypoxia-induced intratumoral heterogeneity. This strategy overcomes the disadvantage of limited penetration of large-sized nanoparticles by enhancing targeting of the normoxic area near tumor blood vessels, and exerting the permeability of small-sized nanoparticles to achieve spatial-targeting of tumor tissue in different depths. Briefly, ultrasmall-sized PAMAM-PR104A (PPA) with tumor penetration characteristics was prepared by conjugating hypoxia-activated prodrug PR104A to

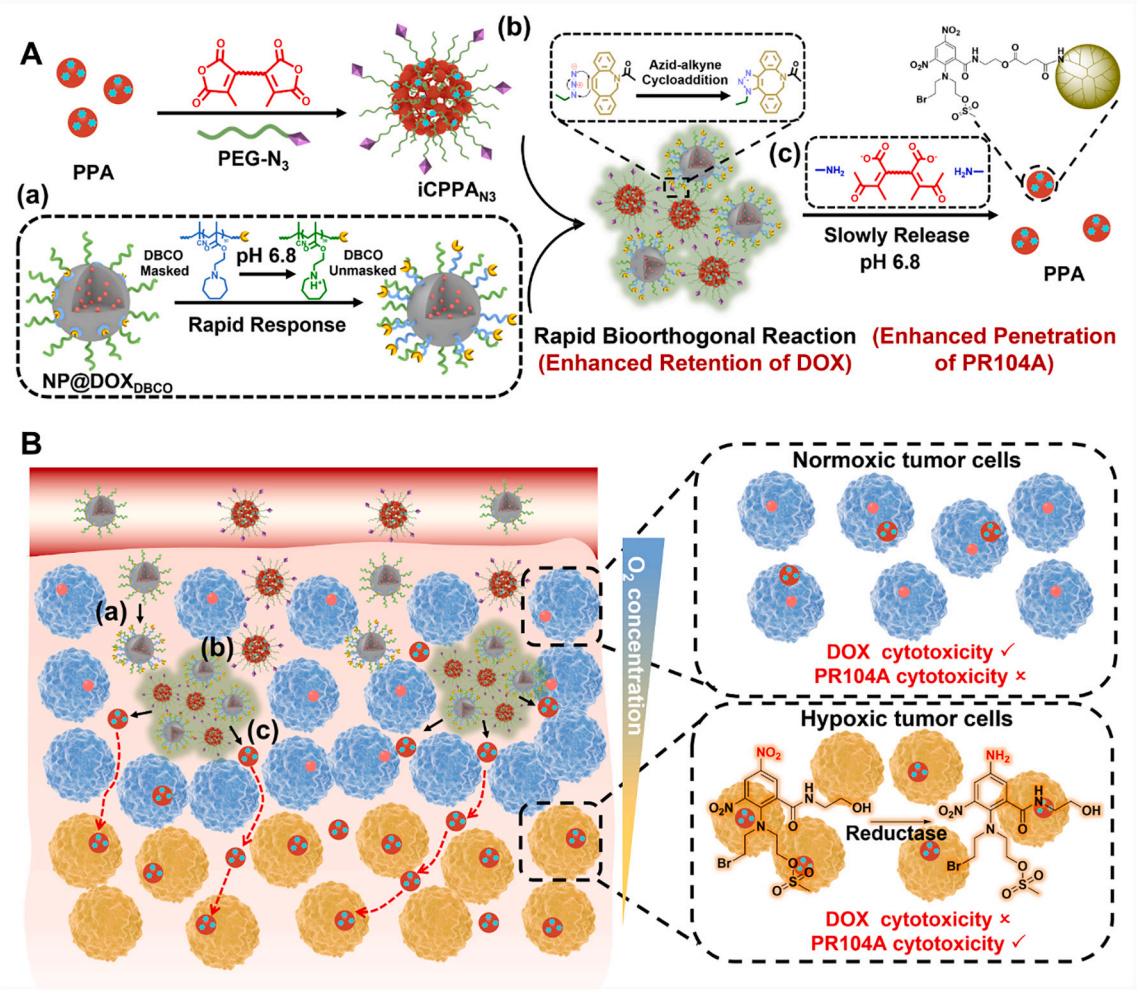

Scheme 1. Schematic illustration of tumor-acidity and bioorthogonal click chemistry-mediated *in situ* size transformable nanocarrier for site-specific combination chemotherapy combating hypoxia-induced intratumoral heterogeneity. (A) Schematic illustration of the preparation of $iCPPA_{N3}$ and the size change of NP@DOX_{DBCO} and $iCPPA_{N3}$ through tumor-acidity and bioorthogonal chemistry. (a) The DBCO group of NP@DOX_{DBCO} quickly exposed due to the rapid tumoral acidity response rate of PAEMA in tumor acidic microenvironment. (b) Cross-linking between NP@DOX_{DBCO} and $iCPPA_{N3}$ to form large-sized drug depots through highly efficient bioorthogonal click reaction for enhanced tumor accumulation. (c) The small-sized PPA slowly released due to the relatively low maleic acid amide response rate and cleaved in tumor acidic microenvironment for enhanced tumor penetration. (B) Schematic illustration of spatial specific delivery of combinational therapeutics for site-specific chemotherapy to combat hypoxia-induced intratumoral heterogeneity.

dendritic poly (amidoamine) (PAMAM). The PPA was further cross-linked with tumor acidity cleavable maleic acid amide linker, and modified with azide (N_3) group through poly(ethylene glycol) (PEG) to form pH-instable PPA cluster (iCPPA$_{N3}$). The DOX-loaded nanoparticles (NP@DOX$_{DBCO}$) were constructed through molecular assembly of poly (caprolactone)-*block*-poly(ethylene glycol) (PCL-*b*-PEG) and dibenzocyclooctyne (DBCO) modified pH-responsive polymer poly(caprolactone)-*block*-poly(2-azepane ethyl methacrylate) (PCL-*b*-PAEMA-DBCO). PAEMA had strong hydrophobicity under normal physiological pH conditions and thus could hide the DBCO group of NP@DOX$_{DBCO}$ to prevent cross-linking between NP@DOX$_{DBCO}$ and iCPPA$_{N3}$. iCPPA$_{N3}$ and NP@DOX$_{DBCO}$ were preferentially accumulated in tumor tissue through enhanced permeability and retention (EPR) effect. The DBCO group of NP@DOX$_{DBCO}$ could be immediately unmasked due to the rapid protonation of PAEMA in tumoral acidity microenvironment (pH 6.5) [45,46], thus reacting with iCPPA$_{N3}$ through the highly efficient bioorthogonal click reaction to form large-sized drug depots (848 nm) for enhanced tumor accumulation and retention, but with limited penetration. The small-sized PPA (10 nm) was further slowly released from the drug depots owing to the relatively low response rate of maleic acid amide in the tumor acidic microenvironment [47], thus enhancing tumor penetration (Scheme 1A). As a result, DOX was accumulated in the normoxic area close to the blood vessel due to limited penetration of large-sized drug depots, which was then preferentially taken to normoxic tumor cells. The small-sized PPA penetrated deep tumor tissues and reached normoxic tumor cells (Scheme 1B). The spatial-specific delivery of combinational therapeutics through *in situ* size transformable nanocarrier can overcome the challenges caused by hypoxia-induced intratumoral heterogeneity, thus realizing synergistic antitumor effect.

2. Experimental section

2.1. Synthesis of PCL-b-PAEMA-DBCO

First, Polycaprolactone (PCL, 0.8 g, 0.12 mmol), 4-Cyano-4-(thiobenzoylthio) pentanoic acid (CPDB, 67.0 mg, 0.24 mol) and 4-dimethylaminopyridine (DMAP, 1.2 mg, 0.01 mol) were dissolved in 5 mL anhydrous dichloromethane (DCM) and then *N,N′*-dicyclohexylcarbodiimide (DCC, 49.4 g, 0.24 mol) in 2 mL anhydrous DCM was added dropwise into a three-neck flask. The solution was reacted for 12 h. After reaction, the solution was filtered to remove the precipitated dicyclohexylurea (DCU) and precipitated in cold diethyl ether three times. The product was dried up under vacuum at room temperature for 24 h and obtained as a pink solid in 81% yield. The product was characterized by ^{1}H NMR.

PCL-*b*-PAEMA were prepared through Reversible Addition-Fragmentation Chain Transfer (RAFT) polymerization. In brief, C7A (379 mg, 1.8 mmol), PCL-CPDB (400 mg, 0.06 mmol), and azobisisobutyronitrile (AIBN, 2.9 mg, 0.018 mmol) were dissolved in *N,N*-dimethylformamide (DMF, 3 mL). After three cycles of freeze-pump-thaw to remove oxygen. The polymerization was carried out at 60 °C for 12 h. After polymerization, the reaction mixture was precipitated in ethyl ether to remove the monomer. The product was collected and dried in the vacuum and obtained as a yellow powder in 86% yield. The product was characterized by ^{1}H NMR.

The terminal thiobenzoylthio group was transferred into thiol to obtain sulfhydryl-terminated PCL-*b*-PAEMA according to previously reported literature [44]. The sulfhydryl-terminated PCL-*b*-PAEMA (0.4 g, 1.0 eqv) was dissolved in anhydrous dioxane under nitrogen atmosphere, and then *N*-(ε-maleimidocaproyloxy) succinimide ester (20 mg, 2.0 eqv) was added into the solution. The mixture was stirred overnight at room temperature. The product PCL-*b*-PAEMA-NHS was purified by precipitating the mixture into ether and drying under vacuum and obtained as a yellow solid in 90% yield. Then, dibenzocyclooctyne-amine (DBCO-NH$_2$, 6.9 mg, 1.0 eqv) and PCL-*b*-PAEMA-NHS (300 mg, 1.0 eqv) were dissolved in DMF and reacted at room temperature for 24 h. The product was further purified by precipitating the mixture into ether and drying under vacuum and obtained as a yellow solid in 85% yield.

2.2. Preparation and characterization of DOX-loaded nanoparticle (NP@DOX$_{DBCO}$)

The DOX-loaded nanoparticle was prepared by nanoprecipitation method [48]. Briefly, a mixture containing PCL-*b*-PEG (8 mg), PCL-*b*-PAEMA-DBCO (2 mg) and DOX (1 mg) was dissolved in 0.5 mL of dimethyl sulfoxide (DMSO), and then gradually added into 5 mL of acidic water (pH ~ 6.0) under stirring for 10 min. After that, pH 7.4 buffer solution was added and stirring for 2 h. The mixture was transferred into dialysis bag (MWCO = 3500) and dialyzed against ultrapure water for 24 h to remove DMSO, and the mixture was filtered through a 0.45 μm filter to obtain NP@DOX$_{DBCO}$. The particle size was measured by dynamic light scattering (DLS) and transmission electron microscope (TEM). The DOX loading efficiency was studied by using fluorescence spectrophotometer. The stability of NP@DOX$_{DBCO}$ in PBS containing 10% FBS was monitored by DLS.

2.3. Preparation and characterization of pH-instable PPA cluster (iCPPA$_{N3}$)

First, the prodrug PR104A was obtained according to previously reported literature [49]. Under N_2 atmosphere, PR104A (249 mg, 0.5 mmol), DCM (5 mL) and succinic anhydride (100 mg, 1 mmol) were mixed. The reaction mixture was stirred for 12 h, then the solvent was removed under reduced pressure. The crude product was purified by silica gel flash chromatography with dichloromethane/methanol at 50:1 to 20:1 to afford the product in 72% yield.

The dendrimer PAMAM G4.0 (56 mg, 1 eqv), *N*-hydroxysuccinimide (NHS, 115 mg, 30 eqv) and PR104A-COOH (48 mg, 20 eqv) were dissolved in anhydrous DMSO under nitrogen atmosphere, and then 1-(3-dimethylaminopropyl)-3-ethylcarbodiimide hydrochloride (EDC, 23 mg, 30 eqv) was added into the solution. The mixture was stirred overnight at room temperature. After reaction, transferred into dialysis bag (MWCO = 3500) and dialyzed against DMSO and then pure water. Finally, the solution was lyophilized to obtain the product in 86% yield.

iCPPA$_{N3}$ was prapared by crosslinking PPA with tumor-acidity-cleavable linker CDM-TEG-CDM. To control nanocluster size, the molar ratio between CDM-containing CDM-TEG-CDM cross-linker and NH_2-containing PAMAM dendrimer was varied. Briefly, CDM-TEG-CDM (1.0 mg mL^{-1} in DMSO) was added dropwise to PPA (10 mg in 4 mL anhydrous DMSO) as predetermined volume. The mixture was stired at room temperature for 8 h. Then a mixture of mPEG$_{2k}$-COOH (2.0 mg, 0.001 mmol), N_3-PEG$_{2k}$-COOH (2.0 mg, 0.001 mmol), NHS (0.29 mg, 0.0025 mmol) and EDC (0.48 mg, 0.0025 mmol) in anhydrous DMSO was added to the above solution. After 24 h, the mixture was dialyzed (MWCO = 7500 Da) against ultrapure water to remove impurities, and the solution was filtered through a 0.45 μm filter to obtain iCPPA$_{N3}$. The pH stable PPA cluster (CPPA$_{N3}$) was prepared though the same method used to develop iCPPA$_{N3}$, except that tumor-acidity-cleavable linker was replaced with pH stable linker CDI-TEG-CDI. The tumor-acidity response decrosslinking of iCPPA$_{N3}$ was detected by using DLS after incubation with PBS at pH 6.5 for different time.

2.4. Crosslinking of iCPPA$_{N3}$ and NP@DOX$_{DBCO}$ in vitro

To verify the click induced crosslinking occurred between NP@DOX$_{DBCO}$ and iCPPA$_{N3}$ under tumor acidity conditions, NP@DOX$_{DBCO}$ and iCPPA$_{N3}$ were mixed in pH 7.4 or pH 6.5 PBS buffer at 37 °C for different time, and the size and morphology changes of the mixed solution were detected by using DLS and TEM.

2.5. In vitro release of PPA

To study the release behavior of PPA from the drug depots constructed by $iCPPA_{N3}$ and $NP@DOX_{DBCO}$, PPA was labeled by rhodamine B (RhB) to obtain PPA_{RhB}. Then, the Cross-linked $iCPPA_{RhB/N3}$ plus $NP@DOX_{DBCO}$ was transferred into dialysis bag (MWCO = 50,000 Da) and was immersed in PBS (pH 7.4 or 6.5, 10 mL) with gentle shaking (80 rpm) at 37 °C. At predetermined time, the external PBS was collected and replaced with fresh PBS. The accumulate released PPA was determined by fluorescence signal intensity of RhB.

2.6. Transwell assay of $iCPPA_{N3}$ plus $NP@DOX_{DBCO}$ in tumor cell monolayer

Mouse breast cancer cells (4 T1) were seeded at 1×10^5 cells/filter on 6.5 mm diameter transwell inserts (poresize ~ 400 nm Corning, NY), which were precoated with 50 μL of matrixgel (BD Biosciences, SanJose, CA). Then, the cells were co-incubated with $iCPPA_{N3/Cy5.5}$ and $NP@DOX_{DBCO}$ in pH 6.5 or 7.4 culture medium for 6 h. After incubation, the cells in flower chamber were collected and determined by Confocal Leser Scanning Microscopy (CLSM) or flow cytometry.

2.7. The combination chemotherapeutic effect of $iCPPA_{N3}$ plus $NP@DOX_{DBCO}$ in multicellular spheroids (MCSs)

We first detect the distribution of DOX and PPA in MCSs. Briefly, the MCSs were divided into four groups randomly and treated with $iCPPA_{Cy5.5/N3}$ plus $NP@DOX_{DBCO}$ or $CPPA_{Cy5.5/N3}$ plus $NP@DOX_{DBCO}$ in pH 6.5 or pH 7.4 medium, respectively. After 8 h, the MCSs were carefully washed with cold PBS and the fluorescence signals of DOX and $PPA_{Cy5.5}$ were observed by CLSM. For combination chemotherapy in MCSs, the MCSs were randomly divided into four groups and treated with $iCPPA_{N3}$ plus $NP@DOX_{DBCO}$ or $CPPA_{N3}$ plus $NP@DOX_{DBCO}$ in pH 6.5 or pH 7.4 medium respectively. After coincubation for 8 h, the medium containing drugs were replaced with fresh medium. After 24 h, MCSs were processed into single cells and treated with annexin V FITC and propidium iodide (PI) sequentially. Then the cells were dispersed in 0.5 mL PBS and analyzed using a flow cytometer.

2.8. In vivo imaging and biodistribution studies

The 4 T1 tumor bearing BALB/c nude mouse were randomly grouped (n = 3), $iCPPA_{N3/Cy5.5}$ plus $NP@DOX_{DBCO}$ or $iCPPA_{Cy5.5}$ plus $NP@DOX_{DBCO}$ was administrated through tail vein injection. The whole-body fluorescence image was collected at a predetermined time using a *in vivo* imaging system (IVIS, Bruker, German). At 36 h post injection, the mice were euthanized, and major organs and tumor tissues were harvested and imaged using the IVIS.

To detect the distribution of DOX and PR104A in tumor tissue, mice bearing 4 T1 tumor were intravenously injected with $iCPPA_{N3/Cy5.5}$ plus $NP@DOX_{DBCO}$ or $CPPA_{N3/Cy5.5}$ plus $NP@DOX_{DBCO}$. After 24 h, the mice were sacrificed, and tumor tissues were excised at 90 min after intravenously injected with Pimonidazole HCl (60 mg kg^{-1}). Tumor tissues were embedded in optimum-cutting temperature (OCT) tissue compound (Sakura, Tokyo, Japan), sectioned into 8 μm slices. After stained hypoxia with fluorescein-conjugated mouse IgG1 monoclonal antibody (MAb clone) (FITC-Mab1) and nuclei with hoechst 33342, the fluorescence of the frozen tumor sections was imaged by CLSM.

2.9. In vivo tumor therapy

The 4 T1 tumor-bearing mice were randomly divided into eight groups (n = 6): (1) PBS, (2) iCP_{N3} (instable PAMAM cluster) plus $NP@_{DBCO}$ (nanoparticles without DOX loaded), (3) DOX, (4) $iCPPA_{N3}$, (5) $NP@DOX_{DBCO}$, (6) iCPPA plus $NP@DOX_{DBCO}$, (7) $iCPPA_{N3}$ plus $NP@DOX_{DBCO}$ and (8) $CPPA_{N3}$ plus $NP@DOX_{DBCO}$. The different formulations were administrated through tail vein injection (5 mg kg^{-1} of DOX, 3 mg kg^{-1} of PR104A) every two days for four times, respectively. The changes of the tumor volumes and body weight were recorded during the treatments. The mice were sacrificed 10 days after the final treatment. Different tissues including heart, liver, spleen, lung, kidney and tumor were harvested and examined using the hematoxylin and eosin (H&E) staining. The cell apoptosis in the tumor tissues was detected using the terminal deoxynucleotidyl transferase dUTP nick-end labeling (TUNEL) assay kits according to the manufacturers' protocols.

2.10. Statistical analysis

All the obtained data were expressed as mean ± standard deviation. Student's t-test was employed for the statistical comparison between the two groups. One-way analysis of variance was employed for statistical comparison among multiple (more than two) groups. "ns" indicates nonsignificant. $^*P < 0.05$, $^{**}P < 0.01$, and $^{***}P < 0.001$ were considered statistically significant in analyses.

3. Results and discussion

3.1. In vitro selective cytotoxic of DOX and PR104A

Hypoxia-induced intratumoral heterogeneity in solid tumors causes different sensitivities of tumor cells to various chemotherapeutics [10,50]. Herein, the selective cytotoxic of DOX and PR104A *in vitro* were determined under different oxygen levels. DOX cytotoxicity in 4 T1 tumor cells decreased in an oxygen level-dependent manner (Fig. S1A-S1C). The IC_{50} value of DOX for 4 T1 cells was decreased by 3.9-folds under hypoxia condition (1% O_2) compared with normoxia condition (21% O_2). In contrast, PR104A cytotoxicity increased with decreasing oxygen levels. The IC_{50} value of PR104A for 4 T1 cells was increased by 5.0-folds under hypoxia condition showed compared with normoxia condition. The trend on mouse colon cancer cells (CT26) is shown in Fig. S1D-S1F. These findings indicate that normoxic tumor cells are more sensitive to DOX, while hypoxic tumors are more sensitive to PR104A. Therefore, the combination of DOX (killing normoxic tumor cells) and PR104A (killing hypoxic tumor cells) can combat hypoxia-induced intratumoral heterogeneity.

3.2. Preparation and characterization of size transformable nanocarrier ($NP@DOX_{DBCO}$ plus $iCPPA_{N3}$)

In this study, a *in situ* size transformable nanocarrier ($NP@DOX_{DBCO}$ plus $iCPPA_{N3}$) was developed to spatially deliver PR104A and DOX to hypoxic and normoxic tumor cells (Fig. 1A, B). To prepare the $NP@DOX_{DBCO}$, poly(caprolactone)-*block*-poly(ethylene glycol) (PCL-*b*-PEG) and PCL-*b*-PAEMA-DBCO were synthesized (Scheme S1), and characterized with ^1H NMR and gel permeation chromatography (GPC) (Fig. S2-S7 and Table S1). The $NP@DOX_{DBCO}$ was prepared *via* a two-step procedure (Fig. 1A) according to previously reported methods [51]. First, PCL-*b*-PAEMA-DBCO, PCL-*b*-PEG, and DOX were self-assembled in a weak acidic (pH 6.5) aqueous solution. Under such conditions, PAEMA showed hydrophilicity due to protonation. The core of obtained nanoparticles was composed of PCL, while the shell was composed of PAEMA-*b*-DBCO and PEG. The aqueous solution was then transformed into physiological environment (pH 7.4), changing PAEMA-*b*-DBCO into a hydrophobic state and collapsing on the core of $NP@DOX_{DBCO}$ to hide the DBCO group. The weight ratio of PCL-*b*-PAEMA-DBCO: PCL-*b*-PEG was optimized as 1:4 based on size and size distribution (Fig. S8A—C). The hydrodynamic diameter of $NP@DOX_{DBCO}$ was measured by using DLS and the morphological was observed *via* a TEM The obtained $NP@DOX_{DBCO}$ with spherical morphology and average diameter was about 100 nm (Fig. 1C), and the loading capacity of DOX was 3.01 ± 0.23%. Long-term stability testing indicated that $NP@DOX_{DBCO}$ had good stability (Fig. S9A). The

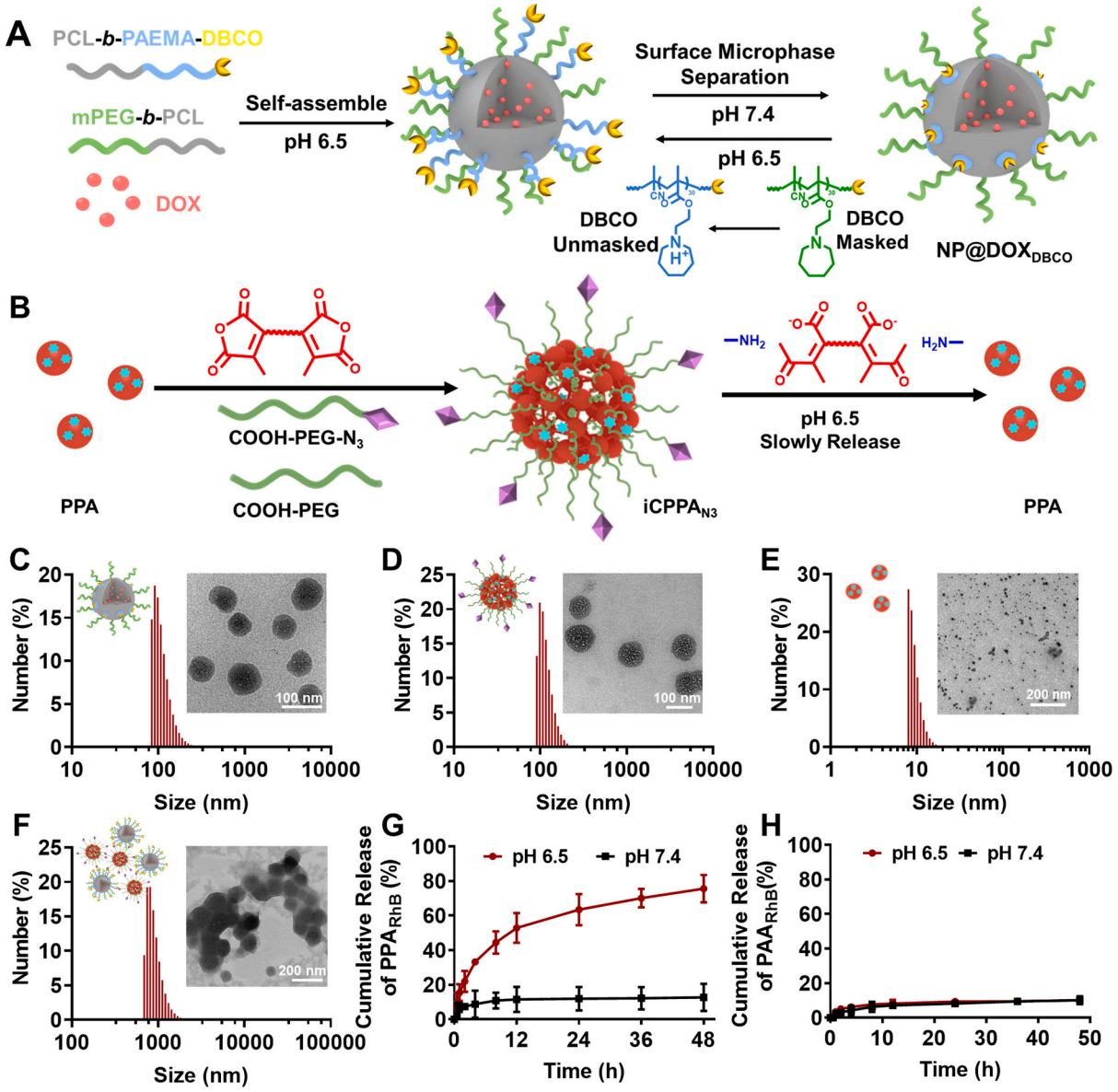

Fig. 1. Preparation and characterization of $NP@DOX_{DBCO}$ and $iCPPA_{N3}$. (A) Schematic diagram of the preparation process of the $NP@DOX_{DBCO}$. (B) Schematic diagram of the preparation process and tumor acidly response release of the $iCPPA_{N3}$. (C) Hydrodynamic size distribution and representative TEM image of $NP@DOX_{DBCO}$. (D) Hydrodynamic size distribution and representative TEM image of $iCPPA_{N3}$. (E) Hydrodynamic size distribution and representative TEM image of $iCPPA_{N3}$ after incubation in pH 6.5 solution for 12 h. (F) Hydrodynamic size distribution and representative TEM image of $NP@DOX_{DBCO}$ plus $iCPPA_{N3}$ after incubation in pH 6.5 solution for 15 min. (G) The release curve of PPA_{RhB} from the drug depots constructed by $NP@DOX_{DBCO}$ and $iCPPA_{N3}$ after incubation in pH 6.5 or pH 7.4 solution for different times. (H) The release curve of PPA_{RhB} from the drug depots constructed by $NP@DOX_{DBCO}$ and $CPPA_{N3}$ after incubation in pH 6.5 or pH 7.4 solution for different times.

accumulative release of DOX was significantly more in a basic medium of pH 6.5 than in the medium of pH 7.4 (Fig. S9B), possibly due to the hydrophilic-hydrophobicity transition of PAEMA and the protonation of DOX. These results indicate that $NP@DOX_{DBCO}$ can effectively deliver DOX into tumor tissue, thus minimizing DOX leakage in blood circulation.

Ultrasmall-sized PPA with tumor penetration ability was prepared by conjugating PR104A to PAMAM (Scheme S2). The ^1H NMR spectroscopy (Fig. S10 and 11) indicates the successful conjugation of PR104A, and the conjugation efficiency of PR104A with PAMAM was 12.8%. Furthermore, PR104A could be released from PPA when the ester bond was hydrolyzed upon the catalysis of esterase (Fig. S13A). PPA was further cross-linked with tumor acidity cleavable linker and modified using α-carboxyl-ω-azido-polyethylene glycol ($COOH\text{-}PEG\text{-}N_3$) to construct pH-instable PPA cluster ($iCPPA_{N3}$) with a size about 100 nm (Fig. 1B), since such nanoparticles enhance passive tumor targeting *via* the EPR effect, and PEG chains can prevent scavenging of the nanoparticles through the macrophage system and reticuloendothelial system by reducing the adsorption of opsonic proteins [41]. The tumor-acidity-cleavable linker CDM-TEG-CDM was synthesized by conjugation of 2,5-dihydro-4-methyl-2,5-dioxo-3-furanpropanoic acid (CDM) and tetraethylene glycol (TEG), due to maleic acid amide in the CDM cleaved under a tumor-acidity environment [52,53]. The products were characterized using ^1H NMR spectroscopy to confirm their structures (Fig. S12). To control nanocluster size, the molar ratio between CDM-containing CDM-TEG-CDM cross-linker and NH_2-containing PAMAM dendrimer was varied. An $iCPPA_{N3}$ with an average size of 104.5 nm could be obtained at a molar ratio of (CDM): (NH_2) of 1:10 (Fig. 1D,

S13B). Moreover, the pH stable PPA cluster ($CPPA_{N3}$) was prepared though the same method used to develop $iCPPA_{N3}$, except that tumor-acidity-cleavable linker was replaced with pH stable linker. The pH-stable linker CDI-TEG-CDI was obtained by *N*, *N*′-carbonyldiimidazole (CDI) activation of TEG. The tumor-acidity response decrosslinked of $iCPPA_{N3}$ was detected by using DLS after incubation with PBS at pH 6.5. The size of $iCPPA_{N3}$ shrank into a small size of about 10 nm after 12 h of incubation (Fig. S13C, Fig. 1E). However, the size change of $CPPA_{N3}$ was negligible at both pH 6.5 and 7.4 (Fig. S13D). These results indicate that $iCPPA_{N3}$ could be efficiently decrosslinked and released small-sized PPA under a tumor-acidity environment.

PAEMA had strong hydrophobicity under physiological environment (pH 7.4) that can hide the DBCO group of $NP@DOX_{DBCO}$ to prevent cross-linking of $NP@DOX_{DBCO}$ and $iCPPA_{N3}$. Moreover, the DBCO group of $NP@DOX_{DBCO}$ was quickly exposed under a tumor acidity environment (pH 6.5) owing to the rapid protonation of PAEMA, thus further reacting with $iCPPA_{N3}$ to form large-sized drug depots [54–57]. To this end, the size change of $NP@DOX_{DBCO}$ and $iCPPA_{N3}$ co-incubation in PBS (pH 7.4 or pH 6.5) was detected by using DLS and TEM. The size significantly increased from 112.0 nm to 848.1 nm after co-incubation in PBS at pH 6.5, indicating that click induced crosslinking occurred under tumor acidity conditions (Fig. S14A, 1F). In contrast, the size of $NP@DOX_{DBCO}$ and $iCPPA_{N3}$ remained constant after co-incubation in PBS or PBS containing 10% fetal bovine serum (FBS) at pH 7.4 (Fig. S14B and 14C), indicating $NP@DOX_{DBCO}$ and $iCPPA_{N3}$ had good stability at physiological conditions. Moreover, to study the pH-response release behavior of PPA from the drug depots constructed by $NP@DOX_{DBCO}$ and $iCPPA_{N3}$, PPA was labeled using RhB to obtain $iCPPA_{N3/RhB}$ and monitored the fluorescent intensity of the fluid outside dialysis bag. As shown in Fig. 1G, the PPA released from the drug depots achieved 74% at pH 6.5 significantly higher than at pH 7.4 (14%) after 48 h. In contrast, the cumulative release of PPA from the drug depots constructed by $NP@DOX_{DBCO}$ and $CPPA_{N3/RhB}$ all lower than 10% under the same environment (Fig. 1H). These results indicate that PPA can be released from the drug depots constructed by $NP@DOX_{DBCO}$ and $iCPPA_{N3}$ under a tumor acidic microenvironment.

3.3. Tissue penetration capacity of PPA

MCSs were used to test whether PPA can improve tissue penetration. MCSs were incubated with $iCPPA_{N3/RhB}$ or $CPPA_{N3/RhB}$ in pH 7.4 or pH 6.5 medium for 8 h and observed using CLSM. For $iCPPA_{N3/RhB}$ treatment, red fluorescence from PPA_{RhB} was distributed throughout the MCSs in pH 6.5 medium, while it was only attached to the periphery of MCSs in pH 7.4 medium (Fig. 2A, S15A). The results indicated that the enhanced penetration of PPA_{RhB} was due to the disintegration of $iCPPA_{N3/RhB}$ in an acidic environment. The released small-sized nanoparticles accelerated movement and diffusion into the deep environment. For $CPPA_{N3/RhB}$ treatment, the fluorescence of PPA_{RhB} was detected at the periphery of the MCSs both in pH 7.4 and 6.5 media (Fig. 2B, S15B) due to the limited penetration of large nanoparticles [41,58]. The enhanced tumor penetration of PPA released from $iCPPA_{N3}$ under tumor acidity conditions was evaluated after co-incubation with *ex vivo* tumor tissues. The *ex vivo* tumor tissues were sliced and observed using CLSM after co-incubation with $iCPPA_{N3/RhB}$ and $CPPA_{N3/RhB}$ in pH 7.4 and pH 6.5 media. The fluorescence signal of PPA_{RhB} had significantly enhanced penetration after incubation with $iCPPA_{N3/RhB}$ in pH 6.5 medium than in pH 7.4 medium (Fig. 2B, S15C and S15D). In contrast, after incubation with $CPPA_{N3/RhB}$ in both pH 6.5 and 7.4 media, the fluorescence signal of RhB was detected at the periphery of tumor tissue. These results show the enhanced penetration capacity of small-sized PPA released from $iCPPA_{N3}$ under tumor acidity, indicating that $iCPPA_{N3}$ can deliver PR104A into deep hypoxic tumor tissues.

A transwell culture system was then established by seeding 4 T1 tumor cells on the membrane insert pre-covered with matrix gel to evaluate the enhanced penetration of PPA released from the drug depots constructed by $iCPPA_{N3}$ and $NP@DOX_{DBCO}$ under acidic conditions (Fig. 2C). PPA was labeled with Cy5.5 to obtain $iCPPA_{N3/Cy5.5}$ and $CPPA_{N3/Cy5.5}$ to facilitate fluorescence detection. The cells in the lower chamber were collected after 6 h of incubation with $iCPPA_{N3/Cy5.5}$ plus $NP@DOX_{DBCO}$ or $CPPA_{N3/Cy5.5}$ plus $NP@DOX_{DBCO}$ in the upper chamber and studied using CLSM or flow analysis. A significantly stronger Cy5.5 fluorescence signals intensity was detected in the cells pretreated with $iCPPA_{N3/Cy5.5}$ plus $NP@DOX_{DBCO}$ in pH 6.5 medium, which mainly attributable to the enhanced penetration capability of PPA released from the drug depots constructed by $iCPPA_{N3/Cy5.5}$ plus $NP@DOX_{DBCO}$ under acidic conditions (Fig. 2D, E). The fluorescence signals intensity of DOX slightly increased in pH 6.5 medium (Fig. 2F), possibly because of the enhanced release of DOX from $NP@DOX_{DBCO}$ under acidic conditions.

3.4. The combination chemotherapeutic effect of $iCPPA_{N3}$ and $NP@DOX_{DBCO}$ in MCSs

The cellular uptake and internalization of $NP@DOX_{DBCO}$, $iCPPA_{N3/Cy5.5}$ and $NP@DOX_{DBCO}$ plus $iCPPA_{N3/Cy5.5}$ was studied by CLSM. The result indicates that $NP@DOX_{DBCO}$ and $iCPPA_{N3/Cy5.5}$ could be efficiently uptake by tumor cells both at pH 7.4 and 6.5 (Fig. S16). In contrast, the fluorescence signals of DOX and Cy5.5 in the 4 T1 cells treated with $NP@DOX_{DBCO}$ plus $iCPPA_{N3/Cy5.5}$ at pH 6.5 all significantly weaker than that at pH 7.4, probably due to inefficient internalization of the formed microscale aggregates under acidic conditions. MTT assay was then used to assess the cytotoxicity of $NP@DOX_{DBCO}$ and $iCPPA_{N3}$ on 4 T1 tumor cells. The cytotoxicity of $NP@DOX_{DBCO}$ was significantly lower in the hypoxia state (IC_{50} = 16.9 μg mL^{-1}) than in the normoxia condition (IC_{50} = 4.6 μg mL^{-1}) due to hypoxia-induced chemoresistance (Fig. 3A). In contrast, $iCPPA_{N3}$ had a higher cell killing effect in hypoxia conditions than in normoxia conditions due to the hypoxia-activated cytotoxicity (IC_{50} = 12.0 μg mL^{-1}) (Fig. 3B). According to our hypothesis, $NP@DOX_{DBCO}$ and $iCPPA_{N3}$ can spatial-specific deliver DOX and PR104A to surface normoxic area and deep hypoxic area, respectively (Fig. 3C). The distribution of DOX and PPA in MCSs after co-incubation with $NP@DOX_{DBCO}$ plus $iCPPA_{N3/Cy5.5}$ in pH 7.4 and 6.5 media for 8 h was studied (Fig. 3D, E). The DOX and Cy5.5 were distributed at the surface of MCSs due to limited penetration of $NP@DOX_{DBCO}$ and $iCPPA_{N3/Cy5.5}$ in pH 7.4. However, the Cy5.5 showed enhanced penetration in pH 6.5 medium, indicating that PPA was released from the drug depots constructed by $NP@DOX_{DBCO}$ plus $iCPPA_{N3/Cy5.5}$, while the DOX was confined in the peripheral region of MCSs. In contrast, DOX and Cy5.5 were distributed in the peripheral region of MCSs in both pH 6.5 and 7.4 media after co-incubation with $NP@DOX_{DBCO}$ plus $CPPA_{N3/Cy5.5}$. These results indicate that this size-switchable nanocarrier can deliver DOX and PR104A to the surface tumor cells and deep tumor cells, respectively.

The cytotoxicity of $NP@DOX_{DBCO}$ combined with $iCPPA_{N3}$ on MCSs was studied to further evaluate the therapeutic effect of the site-specific chemotherapy *in vitro* since MCSs and solid tumors have similar morphology and biological characteristics compared with the single-layer adherent cells [59,60]. Similar to tumors, MCSs have hypoxic and apoptotic/necrotic areas, especially in spheroids with about 500 μm diameter [61–63]. Herein, 3D cell culture plates were used to cultivate MCSs (diameter, about 500 nm) to simulate solid tumors. The MCSs underwent different treatments, then they were digested into single cells for apoptosis analysis (Fig. 3F). $NP@DOX_{DBCO}$ had significant cytotoxicity to MCSs in both pH 7.4 and 6.5 media. The cytotoxicity of $iCPPA_{N3}$ in the pH 6.5 medium was significantly higher than in the pH 7.4 medium, which mainly attributable to the enhanced penetration of PPA and hypoxia-activated cytotoxicity of PR104A in the core of MCSs. The cytotoxicity of $NP@DOX_{DBCO}$ plus $CPPA_{N3}$ was similar to that of $NP@DOX_{DBCO}$, which demonstrated that $CPPA_{N3}$ had negligible toxicity on surface tumor cells. The cytotoxicity of $NP@DOX_{DBCO}$ plus $iCPPA_{N3}$ in the pH 6.5 medium was significantly higher than in other groups, indicating that DOX and PR104A can effectively kill the surface and

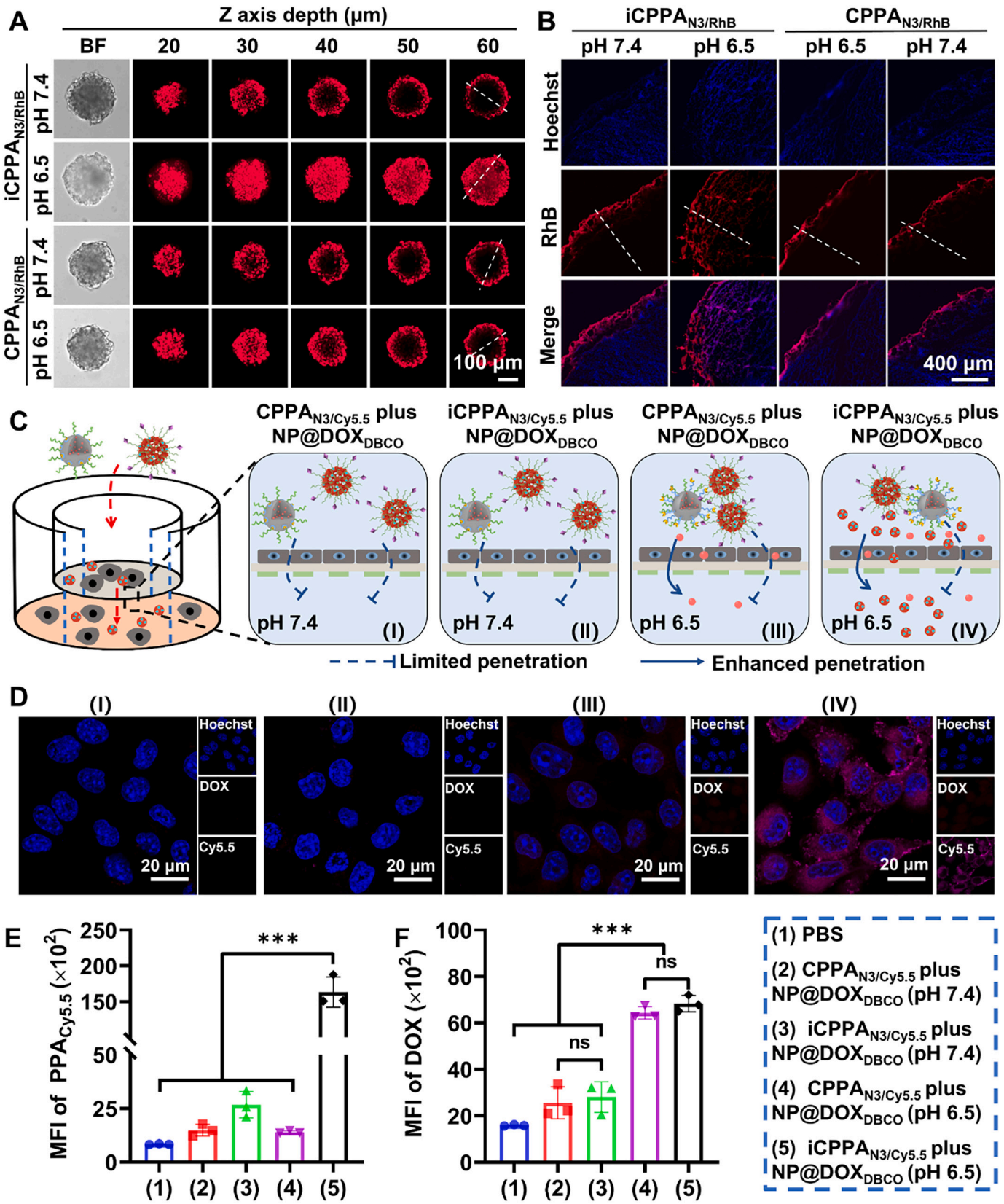

Fig. 2. The tissue penetration capacity of PPA. (A) CLSM observation of MCSs incubated with iCPPA$_{N3/RhB}$ or CPPA$_{N3/RhB}$ in pH 6.5 or pH 7.4 medium for 8 h. (B) CLSM observation of tumor sections after incubation with iCPPA$_{RhB}$ or CPPA$_{RhB}$ in pH 6.5 or pH 7.4 medium. (C) Schematic illustration showing transmigration of iCPPA$_{N3/Cy5.5}$ plus NP@DOX$_{DBCO}$ or CPPA$_{N3/Cy5.5}$ plus NP@DOX$_{DBCO}$ through monolayer 4 T1 cells seeded on the transwell. (D) CLSM images of 4 T1 cells after different treatments in the low chamber. (E) Quantitative analysis of Cy5.5 fluorescence intensity in 4 T1 cells after different treatments in the low chamber. (F) Quantitative analysis of DOX fluorescence intensity in 4 T1 cells after different treatments in the low chamber. Statistical *P*-values: ns $P > 0.05$, ***$P < 0.001$.

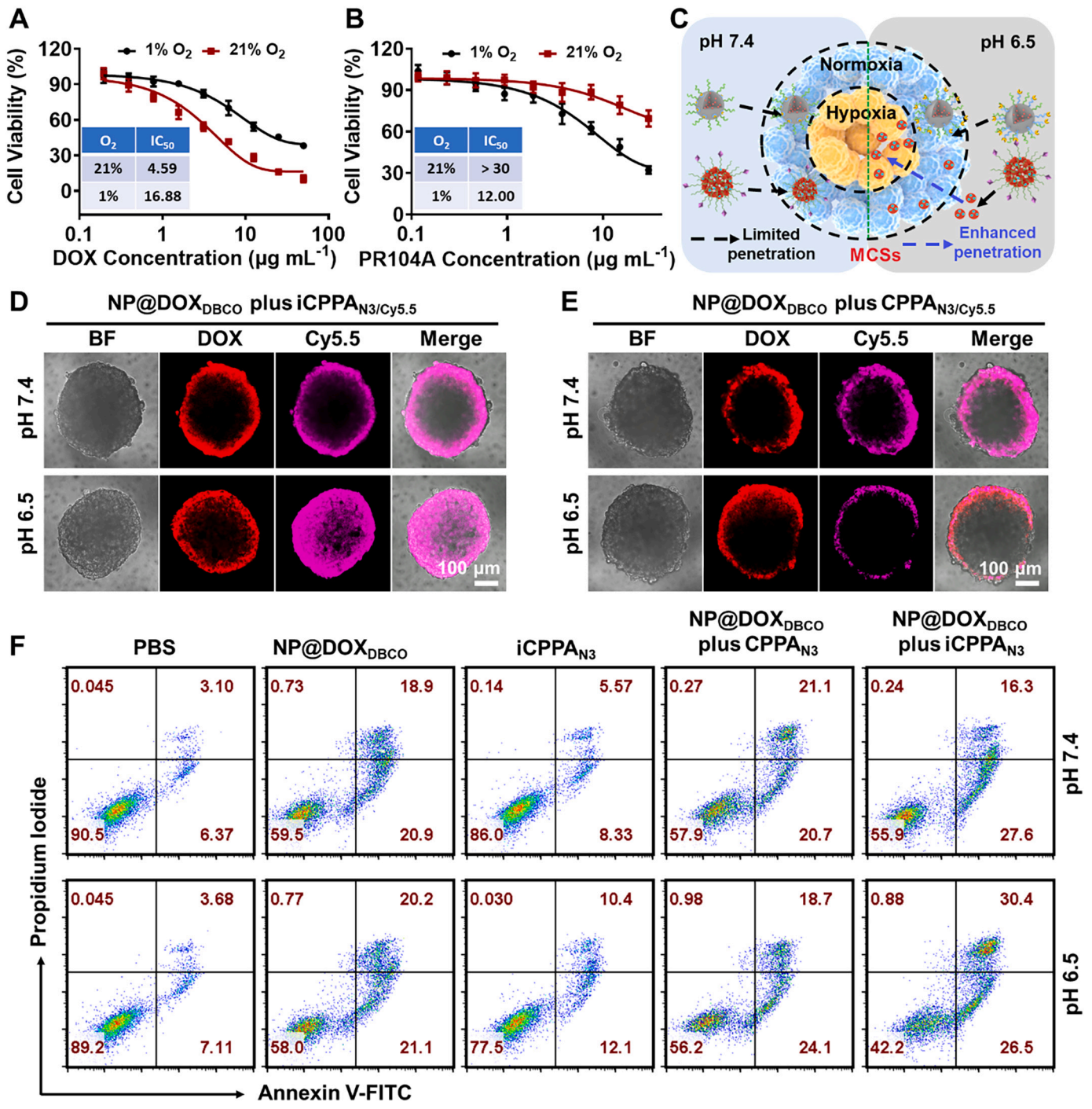

Fig. 3. The combination chemotherapeutic effect in MCSs. (A, B) Cell viability of 4 T1 cells treated with NP@DOX_{DBCO} at different concentrations of DOX (A) or i$CPPA_{N3}$ at different concentrations of PR104A (B) for 24 h under 1% O_2 or 21% O_2 oxygen levels. (C) Schematic illustration showing penetration of NP@DOX_{DBCO} and i$CPPA_{N3}$ at tumor condition (pH 6.5) and normal tissue condition (pH = 7.4). (D, E) CLSM observation of the fluorescence distribution of DOX and Cy5.5 in 4 T1 MCSs incubated with NP@DOX_{DBCO} plus i$CPPA_{N3/Cy5.5}$ (D) or NP@DOX_{DBCO} plus $CPPA_{N3/Cy5.5}$ (E) at pH 6.5 or 7.4 conditions. (F) Flow cytometry analysis of apoptosis in MCSs treated with PBS, NP@DOX_{DBCO}, i$CPPA_{N3}$, NP@DOX_{DBCO} plus i$CPPA_{N3}$ or NP@DOX_{DBCO} plus $CPPA_{N3}$ at pH 6.5 or 7.4 conditions.

deep tumor cells, respectively. In conclusion, a site-specific therapy strategy using different therapeutic modalities to treat the tumor cells at different depths can significantly improve the killing effect of MCSs.

3.5. *In vivo imaging and biodistribution studies*

To confirm our hypothesis that i$CPPA_{N3}$ and NP@DOX_{DBCO} could form large-sized drug depots to enhanced tumor accumulation and retention. 4 T1 tumor-bearing BALB/c nude mice were intravenously injected with Cy5.5 labeled i$CPPA_{N3}$ and NP@DOX_{DBCO}. The biodistribution of i$CPPA_{N3/Cy5.5}$ and NP@DOX_{DBCO} was evaluated using a noninvasive optical imaging technique. Co-administration of i$CPPA_{Cy5.5}$ and NP@DOX_{DBCO} was used as control, due to which showed similar size (~ 110 nm) and zeta potential (~ 9.2 mV) with i$CPPA_{N3/Cy5.5}$ plus NP@DOX_{DBCO} but cannot form large-sized aggregates due to the absence of azide group (N_3). The co-administrated of i$CPPA_{N3/Cy5.5}$ with NP@DOX_{DBCO} significantly enhanced tumor accumulation and retention compared with co-administration of i$CPPA_{Cy5.5}$ and NP@DOX_{DBCO}

(Fig. 4A, B). Furthermore, the major organs of mice at 36 h postinjection were separated for *ex vivo* imaging and quantitatively analyzed (Fig. 4C, D). The fluorescence signals from the tumors of iCPPA$_{N3/Cy5.5}$ plus NP@DOX$_{DBCO}$-treated mice were significantly higher than those of the mice treated with iCPPA$_{Cy5.5}$ plus NP@DOX$_{DBCO}$ group. However, the fluorescence signals were not significantly different in major organs between iCPPA$_{N3/Cy5.5}$ plus NP@DOX$_{DBCO}$ and iCPPA$_{Cy5.5}$ plus NP@DOX$_{DBCO}$ groups. These results indicate that the size transformable nanocarrier of iCPPA$_{N3/Cy5.5}$ plus NP@DOX$_{DBCO}$ can enhance tumor accumulation and retention.

Immunofluorescence staining was conducted on tumor sections after intravenous injection with iCPPA$_{N3}$ plus NP@DOX$_{DBCO}$ or CPPA$_{N3}$ plus NP@DOX$_{DBCO}$ for 24 h using CLSM to further investigate the distribution of DOX and PPA in tumor tissues. The hypoxia area was marked using pimonidazole HCl and stained with fluorescein-conjugated mouse IgG1 monoclonal antibody (MAb clone) (FITC-Mab1). PPA was uniformly perfused into the hypoxic tumor tissue after treatment with iCPPA$_{N3}$ plus NP@DOX$_{DBCO}$, while DOX was not found in hypoxic tissues (Fig. 4E). In contrast, the fluorescence signals of DOX and PPA were outside the hypoxic areas after treatment with CPPA$_{N3}$ plus

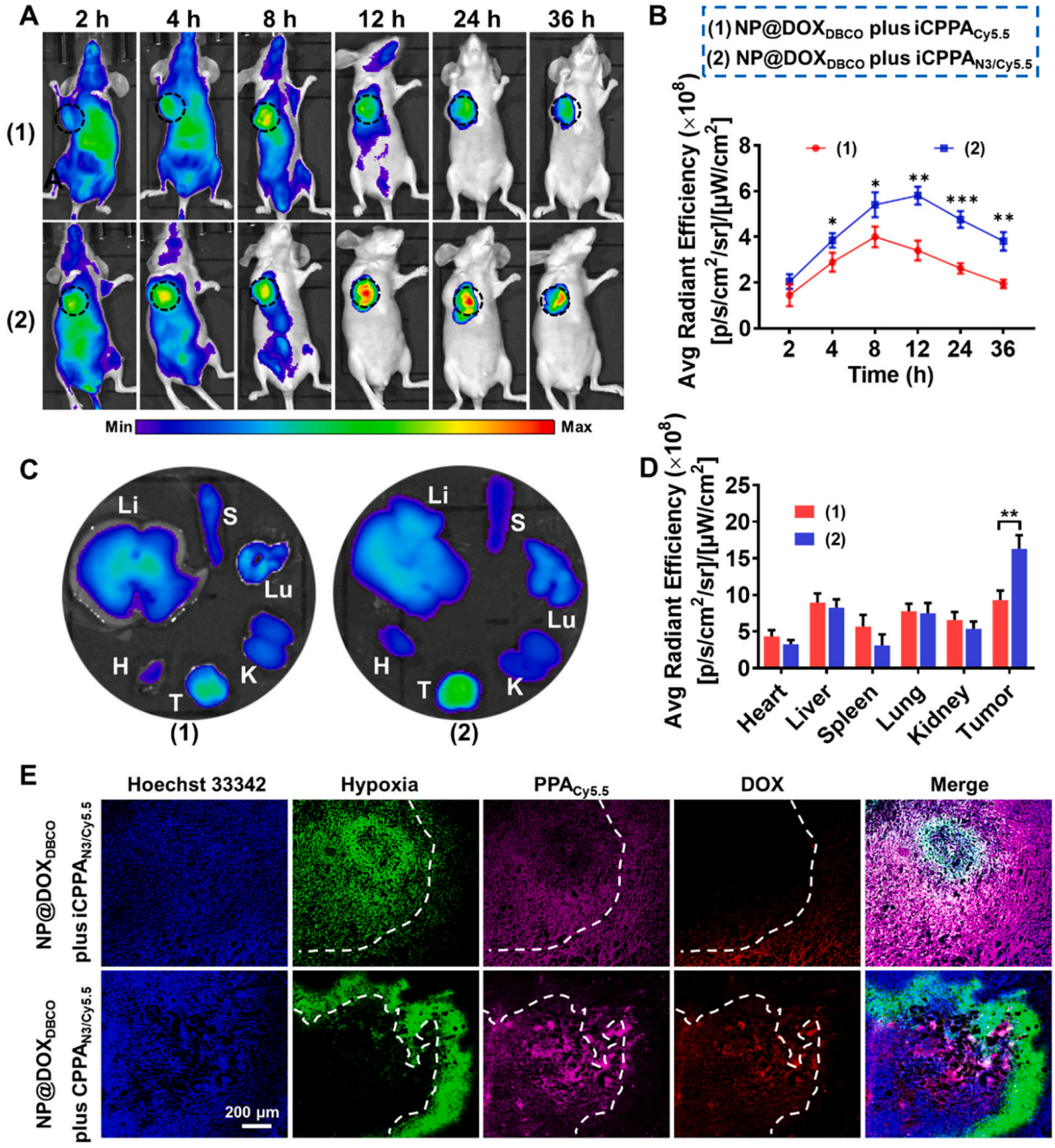

Fig. 4. *In vivo* imaging and biodistribution studies. (A) *In vivo* fluorescence images of 4 T1 tumor-bearing mice taken at different time points after intravenous injection of iCPPA$_{Cy5.5/N3}$ plus NP@DOX$_{DBCO}$ or iCPPA$_{Cy5.5}$ plus NP@DOX$_{DBCO}$. (B) Quantification of fluorescence intensities in tumor site over time in (A). (C) *Ex vivo* fluorescence images of major organs (heart, liver, spleen, lung, and kidney) and tumors taken 36 h after injection from (A). (D) Quantified fluorescence intensity of tumors based on the *ex vivo* fluorescence images in (C). (E) CLSM immunofluorescence images showing fluorescence distribution of DOX and PPA$_{Cy5.5}$ in tumor tissue after injection with iCPPA$_{Cy5.5/N3}$ plus NP@DOX$_{DBCO}$ or CPPA$_{Cy5.5/N3}$ plus NP@DOX$_{DBCO}$. Hypoxyprobe™-1 PLUS kit was used to label the hypoxia area. Statistical *P*-values: $^{*}P < 0.05$, $^{**}P < 0.01$, $^{***}P < 0.001$.

$NP@DOX_{DBCO}$. These results suggest that the size-switchable nanosystem can spatially deliver hypoxia-activated prodrugs PR104A and DOX to hypoxic and normoxic tumor cells.

3.6. *In vivo* therapeutic efficacy

Inspired by the superior performance of $iCPPA_{N3}$ plus $NP@DOX_{DBCO}$ *in vitro* and *in vivo* studies, the *in vivo* therapeutic efficacy of $iCPPA_{N3}$

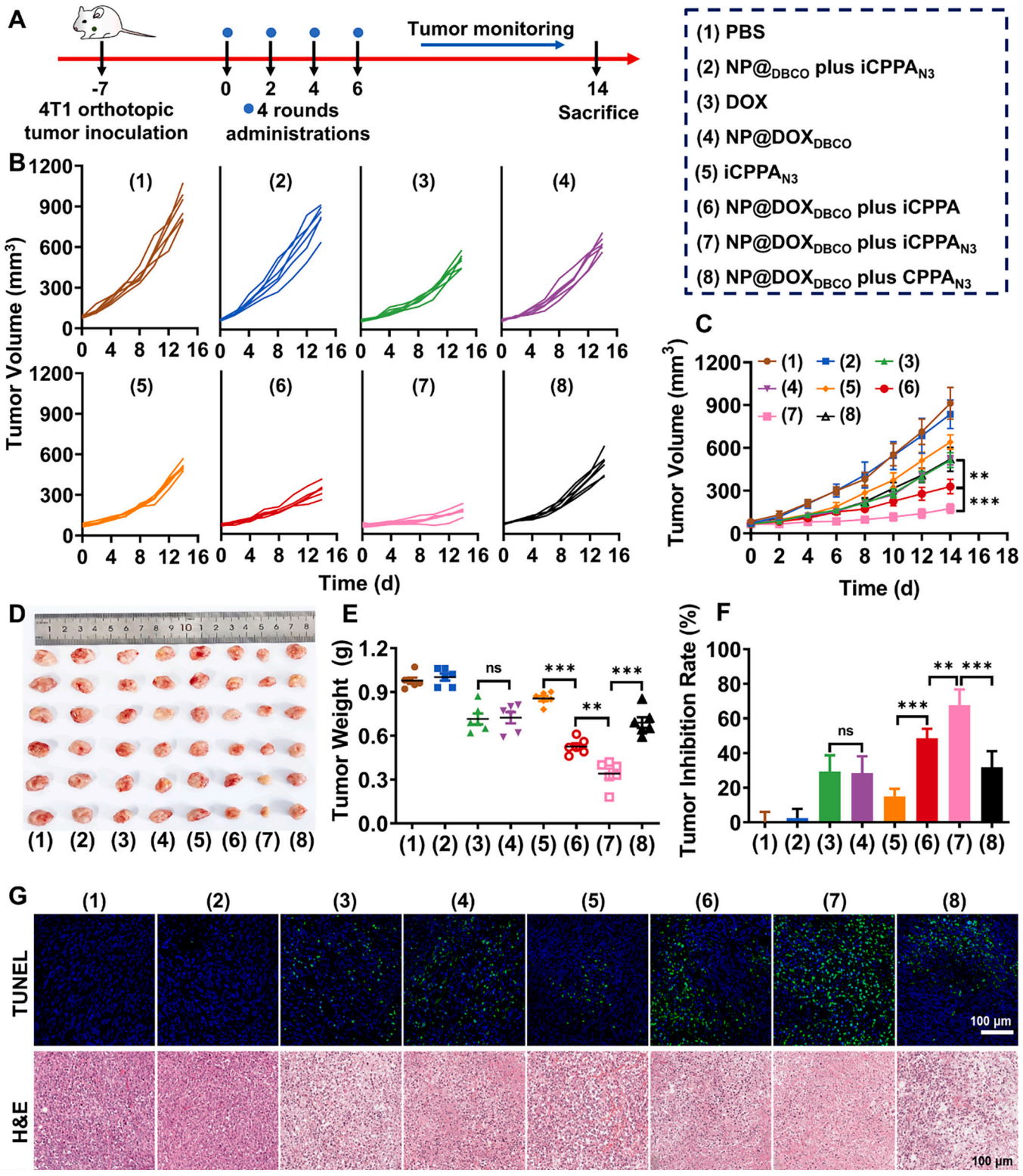

Fig. 5. *In vivo* anti-tumor effect. (A) Schematics of the treatment schedule. (B) Spaghetti plots of 4 T1 tumor growth after various treatments. (C) Relative tumor volumes of mice after different treatments. (D) The images of the tumors at the end of antitumor study. (E) The weights of the tumors after different treatments at the end of antitumor study. (F) Tumor inhibition ratio. (G) TUNEL and H&E staining of the tumor sections after different treatments for 14 d. Statistical *P*-values: ns $P > 0.05$, $^{**}P < 0.01$, $^{***}P < 0.001$.

plus NP@DOX_{DBCO} was compared with that of PBS, iCP_{N3} (instable PAMAM cluster) plus NP@$_{DBCO}$ (nanoparticles without DOX loaded), DOX, $iCPPA_{N3}$, NP@DOX_{DBCO}, iCPPA plus NP@DOX_{DBCO}, $iCPPA_{N3}$ plus NP@DOX_{DBCO} and $CPPA_{N3}$ plus NP@DOX_{DBCO} in mice with 4 T1 tumors (Fig. 5A). The tumor growth curves for all the groups are plotted in Fig. 5B, C, the tumor volumes in PBS and iCP_{N3} plus NP@$_{DBCO}$-treated groups sharply increased during treatment, indicating the insignificant tumor suppression of iCP_{N3} plus NP@$_{DBCO}$. DOX, $iCPPA_{N3}$, NP@DOX_{DBCO}, $CPPA_{N3}$ plus NP@DOX_{DBCO} treatment showed slight tumor inhibition, iCPPA plus NP@DOX_{DBCO} treatment showed significantly enhanced tumor growth inhibition, and the administration of $iCPPA_{N3}$ plus NP@DOX_{DBCO} almost completely suppressed tumor growth. After treatment, the mice were sacrificed, and excised tumor tissues were imaged and weighted (Fig. 5D, E) to visually confirm the best anticancer activity after NP@DOX_{DBCO} plus $iCPPA_{N3}$ treatment. The tumor inhibition rates were further calculated to evaluate therapeutic effects of different treatments (Fig. 5F). The NP@DOX_{DBCO} plus $iCPPA_{N3}$ group with a tumor inhibition rate of 67.7%, significantly higher than DOX (29.4%), NP@DOX_{DBCO} (28.5%), $iCPPA_{N3}$ (15.0%), NP@DOX_{DBCO} plus iCPPA (48.6%) and NP@DOX_{DBCO} plus $CPPA_{N3}$ (31.9%). Moreover, H&E staining and TUNEL staining also revealed that $iCPPA_{N3}$ plus NP@DOX_{DBCO} treatment caused the highest level of anticancer activity (Fig. 5G). The superior therapeutic effect of the NP@DOX_{DBCO} plus $iCPPA_{N3}$ group was mainly due to the spatial specific delivery of combinational therapeutics in tumor situ. In addition, the negligible change in body weight during the treatment (Fig. S17) and H&E staining of the main organs at the end of treatment showed no significant tissue damage (Fig. S18). Moreover, the hematological indexes at 7 days after systemic delivery of $iCPPA_{N3}$ plus NP@DOX_{DBCO} showed no significant difference compared with those of the PBS group (Fig. S19). These results indicate that $iCPPA_{N3}$ plus NP@DOX_{DBCO}-induced antitumor therapy is highly biocompatible.

4. Conclusion

In this study, a *in situ* size transformable nanocarrier (NP@DOX_{DBCO} plus $iCPPA_{N3}$) with spatial specific delivery of combinational therapeutics was designed to combat hypoxia-induced intratumoral heterogeneity. *In vitro* and *in vivo* experiments demonstrated that NP@DOX_{DBCO} and $iCPPA_{N3}$ could form large-sized drug depots under tumor acidic microenvironment and enhance tumor accumulation and retention. The ultrasmall-sized PPA with tumor penetration characteristics was released from the drug depots to deliver PR104A to the deep hypoxic area of the tumor tissues. The site-specific chemotherapy combination of DOX and PR104A can kill the surface normoxic and deep hypoxic tumor cells, respectively, indicating excellent antitumor efficiency. Overall, the site-specific combination therapy strategy using different therapeutics to treat various tumor cells may provide tailored tumor therapy.

Author contributions

K. W. and M. J. contributed equally to this work. K.W., M. J.and Y.Y. designed and performed the project. K.W. and Y.Y. analyzed the data. J. Z., Y.D., Y.L., and Q.Z. assisted with experiments. K. W., P. S., S. P. and Y. Y. prepared and wrote the final version of the manuscript.

CRediT authorship contribution statement

Kewei Wang: Conceptualization, Methodology, Software, Writing – original draft. **Maolin Jiang:** Conceptualization, Methodology, Writing – original draft. **Jielian Zhou:** Methodology, Validation. **Yansong Dong:** Methodology, Validation. **Ye Liu:** Methodology, Validation. **Qingyu Zong:** Methodology. **Puja Sandbhor:** Writing – review & editing. **N.D. Pradeep Singh:** Writing – review & editing. **Youyong Yuan:** Funding acquisition, Conceptualization, Writing – review & editing.

Declaration of Competing Interest

The authors declare that they have no known competing financial interests or personal relationships that could have appeared to influence the work reported in this paper.

Acknowledgements

This work was supported by the National Natural Science Foundation of China (51873072, 52073101); the Science and Technology Program of Guangzhou (202102010025); Guangdong Provincial Pearl River Talents Program (2019QN01Y088); the Special Fund for the Construction of High-level Key Clinical Specialty (Medical Imaging) in Guangzhou; Guangzhou Key Laboratory of Molecular Imaging and Clinical Translational Medicine; Guangdong Basic and Applied Basic Research Foundation (2021A1515110258); Open Fund of Key Laboratory of Biomaterials of Guangdong Higher Education Institutes and Guangdong Provincial Engineering and Technological Research Center for Drug Carrier Development.

Appendix A. Supplementary data

Supplementary data to this article can be found online at https://doi.org/10.1016/j.jconrel.2022.06.046.

References

[1] I. Dagogo-Jack, A.T. Shaw, Tumour heterogeneity and resistance to cancer therapies, Nat. Rev. Clin. Oncol. 15 (2) (2018) 81–94.
[2] C.E. Meacham, S.J. Morrison, Tumour heterogeneity and cancer cell plasticity, Nature 501 (7467) (2013) 328–337.
[3] P.L. Bedard, A.R. Hansen, M.J. Ratain, L.L. Siu, Tumour heterogeneity in the clinic, Nature 501 (7467) (2013) 355–364.
[4] M.R. Junttila, F.J. de Sauvage, Influence of tumour micro-environment heterogeneity on therapeutic response, Nature 501 (7467) (2013) 346–354.
[5] K.K. Reza, S. Dey, A. Wuethrich, W. Jing, A. Behren, F. Antaw, Y. Wang, A.A. Sina, M. Trau, In situ single cell proteomics reveals circulating tumor cell heterogeneity during treatment, ACS Nano 15 (7) (2021) 11231–11243.
[6] S. Shen, X. Xu, S. Lin, Y. Zhang, H. Liu, C. Zhang, R. Mo, A nanotherapeutic strategy to overcome chemotherapeutic resistance of cancer stem-like cells, Nat. Nanotechnol. 16 (1) (2021) 104–113.
[7] L.C. Demmers, K. Kretzschmar, A. Van Hoeck, Y.E. Bar-Epraim, H.W.P. van den Toorn, M. Koomen, G. van Son, J. van Gorp, A. Pronk, N. Smakman, E. Cuppen, H. Clevers, A.J.R. Heck, W. Wu, Single-cell derived tumor organoids display diversity in HLA class I peptide presentation, Nat. Commun. 11 (1) (2020) 5338.
[8] K.M. Ihsanullah, B.N. Kumar, Y. Zhao, H. Muhammad, Y. Liu, L. Wang, H. Liu, W. Jiang, Stepwise-activatable hypoxia triggered nanocarrier-based photodynamic therapy for effective synergistic bioreductive chemotherapy, Biomaterials 245 (2020), 119982.
[9] W.R. Wilson, M.P. Hay, Targeting hypoxia in cancer therapy, Nat. Rev. Cancer 11 (6) (2011) 393–410.
[10] X. Xin, V. Kumar, F. Lin, V. Kumar, R. Bhattarai, V.R. Bhatt, C. Tan, R.I. Mahato, Redox-responsive nanoplatform for codelivery of miR-519c and gemcitabine for pancreatic cancer therapy, Sci. Adv. 6 (46) (2020) eabd6764.
[11] J.T. Xu, W. Han, P.P. Yang, T. Jia, S.M. Dong, H.T. Bi, A. Gulzar, D. Yang, S.L. Gai, F. He, J. Lin, C.X. Li, Tumor microenvironment-responsive mesoporous MnO2-coated upconversion nanoplatform for self-enhanced tumor theranostics, Adv. Funct. Mater. 28 (36) (2018) 1803804.
[12] A. Sahu, I. Kwon, G. Tae, Improving cancer therapy through the nanomaterials-assisted alleviation of hypoxia, Biomaterials 228 (2020), 119578.
[13] H. Yang, H. Zhang, Y. Yang, X. Wang, T. Deng, R. Liu, T. Ning, M. Bai, H. Li, K. Zhu, J. Li, Q. Fan, G. Ying, Y. Ba, Hypoxia induced exosomal circRNA promotes metastasis of colorectal cancer via targeting GEF-H1/RhoA axis, Theranostics 10 (18) (2020) 8211–8226.
[14] A. Stadlbauer, M. Zimmermann, A. Doerfler, S. Oberndorfer, M. Buchfelder, R. Coras, M. Kitzwogerer, K. Roessler, Intratumoral heterogeneity of oxygen metabolism and neovascularization uncovers 2 survival-relevant subgroups of IDH1 wild-type glioblastoma, Neuro-Oncology 20 (11) (2018) 1536–1546.
[15] X. Cao, S. Rao Allu, S. Jiang, M. Jia, J.R. Gunn, C. Yao, E.P. LaRochelle, J.R. Shell, P. Bruza, D.J. Gladstone, L.A. Jarvis, J. Tian, S.A. Vinogradov, B.W. Pogue, Tissue pO2 distributions in xenograft tumors dynamically imaged by Cherenkov-excited phosphorescence during fractionated radiation therapy, Nat. Commun. 11 (1) (2020) 573.
[16] J. Li, A. Chekkoury, J. Prakash, S. Glasl, P. Vetschera, B. Koberstein-Schwarz, I. Olefir, V. Gujrati, M. Omar, V. Ntziachristos, Spatial heterogeneity of

oxygenation and haemodynamics in breast cancer resolved in vivo by conical multispectral optoacoustic mesoscopy, Light Sci. Appl. 9 (2020) 57.
[17] A. Sharma, J.F. Arambula, S. Koo, R. Kumar, H. Singh, J.L. Sessler, J.S. Kim, Hypoxia-targeted drug delivery, Chem. Soc. Rev. 48 (3) (2019) 771–813.
[18] H. Zhou, F. Qin, C. Chen, Designing hypoxia-responsive nanotheranostic agents for tumor imaging and therapy, Adv. Healthc Mater. 10 (5) (2021), e2001277.
[19] D. Huo, X. Jiang, Y. Hu, Recent advances in nanostrategies capable of overcoming biological barriers for tumor management, Adv. Mater. 32 (27) (2020), e1904337.
[20] C.D. Phung, T.H. Tran, L.M. Pham, H.T. Nguyen, J.H. Jeong, C.S. Yong, J.O. Kim, Current developments in nanotechnology for improved cancer treatment, focusing on tumor hypoxia, J. Control. Release 324 (2020) 413–429.
[21] H. Wang, J. Li, Y.Q. Wang, X. Gong, X.X. Xu, J.Y. Wang, Y.P. Li, X.Y. Sha, Z. W. Zhang, Nanoparticles-mediated reoxygenation strategy relieves tumor hypoxia for enhanced cancer therapy, J. Control. Release 319 (2020) 25–45.
[22] N. Rohwer, T. Cramer, Hypoxia-mediated drug resistance: novel insights on the functional interaction of HIFs and cell death pathways, Drug Resist. Updat. 14 (3) (2011) 191–201.
[23] D. Samanta, D.M. Gilkes, P. Chaturvedi, L. Xiang, G.L. Semenza, Hypoxia-inducible factors are required for chemotherapy resistance of breast cancer stem cells, Proc. Natl. Acad. Sci. U. S. A. 111 (50) (2014) E5429–E5438.
[24] H.O. Alsaab, S. Sau, R.M. Alzhrani, V.T. Cheriyan, L.A. Polin, U. Vaishampayan, A. K. Rishi, A.K. Iyer, Tumor hypoxia directed multimodal nanotherapy for overcoming drug resistance in renal cell carcinoma and reprogramming macrophages, Biomaterials 183 (2018) 280–294.
[25] F. Li, H. Mei, Y. Gao, X. Xie, H. Nie, T. Li, H. Zhang, L. Jia, Co-delivery of oxygen and erlotinib by aptamer-modified liposomal complexes to reverse hypoxia-induced drug resistance in lung cancer, Biomaterials 145 (2017) 56–71.
[26] C.Q. Qiao, X.F. Wang, G.H. Liu, Z. Yang, Q. Jia, L.X. Wang, R.L. Zhang, Y.Q. Xia, Z. L. Wang, Y. Yang, Erythrocyte membrane camouflaged metal-organic framework nanodrugs for remodeled tumor microenvironment and enhanced tumor chemotherapy, Adv. Funct. Mater. 2107791 (2021).
[27] Y.N. Yang, Y. Lu, P.L. Abbaraju, I. Azimi, C. Lei, J. Tang, M. Jambhrunkar, J.Y. Fu, M. Zhang, Y. Liu, C. Liu, C.Z. Yu, Stepwise degradable nanocarriers enabled cascade delivery for synergistic cancer therapy, Adv. Funct. Mater. 28 (28) (2018) 1800706.
[28] H.H. Yin, B.G. Zhou, C.K. Zhao, L.P. Sun, W.W. Yue, X.L. Li, H.Y. Li, S.Y. Li, H. X. Xu, Y. Chen, 2D core/shell-structured mesoporous silicene@silica for targeted and synergistic NIR-II-induced photothermal ablation and hypoxia-activated chemotherapy of tumor, Adv. Funct. Mater. 31 (24) (2021) 2102043.
[29] S. Yang, Z. Tang, C. Hu, D. Zhang, N. Shen, H. Yu, X. Chen, Selectively potentiating hypoxia levels by combretastatin A4 nanomedicine: toward highly enhanced hypoxia-activated prodrug tirapazamine therapy for metastatic tumors, Adv. Mater. 31 (11) (2019), e1805955.
[30] J. Wang, S. Shen, J. Li, Z. Cao, X. Yang, Precise depletion of tumor seed and growing soil with shrinkable nanocarrier for potentiated cancer chemoimmunotherapy, ACS Nano 15 (3) (2021) 4636–4646.
[31] S. Wang, P. Huang, X.Y. Chen, Hierarchical targeting strategy for enhanced tumor tissue accumulation/retention and cellular internalization, Adv. Mater. 28 (34) (2016) 7340–7364.
[32] Y.L. Su, T.W. Yu, W.H. Chiang, H.C. Chiu, C.H. Chang, C.S. Chiang, S.H. Hu, Hierarchically targeted and penetrated delivery of drugs to tumors by size-changeable graphene quantum dot nanoaircrafts for photolytic therapy, Adv. Funct. Mater. 27 (23) (2017) 1700056.
[33] J. Shi, P.W. Kantoff, R. Wooster, O.C. Farokhzad, Cancer nanomedicine: progress, challenges and opportunities, Nat. Rev. Cancer 17 (1) (2017) 20–37.
[34] H. Phuengkham, L. Ren, I.W. Shin, Y.T. Lim, Nanoengineered immune niches for reprogramming the immunosuppressive tumor microenvironment and enhancing cancer immunotherapy, Adv. Mater. 31 (34) (2019), e1803322.
[35] Q. Sun, Z. Zhou, N. Qiu, Y. Shen, Rational design of cancer nanomedicine: nanoproperty integration and synchronization, Adv. Mater. 29 (14) (2017) 1606628.
[36] J. Yan, N. Zhang, Z. Zhang, W. Zhu, B. Li, L. Li, Y. Pu, B. He, Redox-responsive polyethyleneimine/tetrahedron DNA/doxorubicin nanocomplexes for deep cell/tissue penetration to overcome multidrug resistance, J. Control. Release 329 (2021) 36–49.
[37] H.S. El-Sawy, A.M. Al-Abd, T.A. Ahmed, K.M. El-Say, V.P. Torchilin, Stimuli-responsive nano-architecture drug-delivery systems to solid tumor micromilieu: past, present, and future perspectives, ACS Nano 12 (11) (2018) 10636–10664.
[38] M. Souri, M. Soltani, F.M. Kashkooli, M.K. Shahvandi, Engineered strategies to enhance tumor penetration of drug-loaded nanoparticles, J. Control. Release 341 (2022) 227–246.
[39] W.F. Jia, Y.S. Wang, R. Liu, X.R. Yu, H.L. Gao, Shape transformable strategies for drug delivery, Adv. Funct. Mater. 31 (18) (2021) 2009765.
[40] W. Yu, R. Liu, Y. Zhou, H. Gao, Size-tunable strategies for a tumor targeted drug delivery system, ACS Cent. Sci. 6 (2) (2020) 100–116.
[41] H. Cabral, Y. Matsumoto, K. Mizuno, Q. Chen, M. Murakami, M. Kimura, Y. Terada, M.R. Kano, K. Miyazono, M. Uesaka, N. Nishiyama, K. Kataoka, Accumulation of sub-100 nm polymeric micelles in poorly permeable tumours depends on size, Nat. Nanotechnol. 6 (12) (2011) 815–823.
[42] H.J. Li, J.Z. Du, X.J. Du, C.F. Xu, C.Y. Sun, H.X. Wang, Z.T. Cao, X.Z. Yang, Y. H. Zhu, S. Nie, J. Wang, Stimuli-responsive clustered nanoparticles for improved tumor penetration and therapeutic efficacy, Proc. Natl. Acad. Sci. U. S. A. 113 (15) (2016) 4164–4169.
[43] L. Wang, W. Jiang, L. Xiao, H. Li, Z. Chen, Y. Liu, J. Dou, S. Li, Q. Wang, W. Han, Y. Wang, H. Liu, Self-reporting and splitting nanopomegranates potentiate deep tissue cancer radiotherapy via elevated diffusion and transcytosis, ACS Nano 14 (7) (2020) 8459–8472.
[44] M. Li, P. De, S.R. Gondi, B.S. Sumerlin, End group transformations of RAFT-generated polymers with bismaleimides: functional telechelics and modular block copolymers, J. Polym. Sci. A Polym. Chem. 46 (15) (2008) 5093–5100.
[45] K. Wang, M. Jiang, J. Zhou, Y. Liu, Q. Zong, Y. Yuan, Tumor-acidity and bioorthogonal chemistry-mediated on-site size transformation clustered nanosystem to overcome hypoxic resistance and enhance chemoimmunotherapy, ACS Nano 16 (1) (2022) 721–735.
[46] H.J. Li, J.Z. Du, J. Liu, X.J. Du, S. Shen, Y.H. Zhu, X.Y. Wang, X.D. Ye, S.M. Nie, J. Wang, Smart superstructures with ultrahigh pH-sensitivity for targeting acidic tumor microenvironment: instantaneous size switching and improved tumor penetration, ACS Nano 10 (7) (2016) 6753–6761.
[47] J.Z. Du, H.J. Li, J. Wang, Tumor-acidity-cleavable maleic acid amide (TACMAA): a powerful tool for designing smart nanoparticles to overcome delivery barriers in cancer nanomedicine, Acc. Chem. Res. 51 (11) (2018) 2848–2856.
[48] M. Jiang, K. Wang, X. Xiao, Q. Zong, R. Zheng, Y. Yuan, Theranostic heterodimeric prodrug with dual-channel fluorescence turn-on and dual-prodrug activation for synergistic cancer therapy, Adv. Healthc Mater. 10 (21) (2021), e2101144.
[49] S.J. Yang, G.J. Atwell, W.A. Denny, Synthesis of asymmetric halomesylate mustards with aziridineethanol/alkali metal halides: application to an improved synthesis of the hypoxia prodrug PR-104, Tetrahedron 63 (25) (2007) 5470–5476.
[50] K. Graham, E. Unger, Overcoming tumor hypoxia as a barrier to radiotherapy, chemotherapy and immunotherapy in cancer treatment, Int. J. Nanomedicine 13 (2018) 6049–6058.
[51] X. Li, X. Cai, Z. Zhang, Y. Ding, R. Ma, F. Huang, Y. Liu, J. Liu, L. Shi, Mimetic heat shock protein mediated immune process to enhance cancer immunotherapy, Nano Lett. 20 (6) (2020) 4454–4463.
[52] K. Yang, S. Zhang, G. Zhang, X. Sun, S.T. Lee, Z. Liu, Graphene in mice: ultrahigh in vivo tumor uptake and efficient photothermal therapy, Nano Lett. 10 (9) (2010) 3318–3323.
[53] H. Wang, X. Xu, X. Guan, S. Shen, X. Huang, G. Kai, S. Zhao, W. Ruan, L. Zhang, T. Pang, R. Mo, Liposomal 9-Aminoacridine for treatment of ischemic stroke: from drug discovery to drug delivery, Nano Lett. 20 (3) (2020) 1542–1551.
[54] Y. Dong, Y. Tu, K. Wang, C. Xu, Y. Yuan, J. Wang, A general strategy for macrotheranostic prodrug activation: synergy between the acidic tumor microenvironment and bioorthogonal chemistry, Angew. Chem. Int. Ed. Eng. 59 (18) (2020) 7168–7172.
[55] Y. Tu, Y. Dong, K. Wang, S. Shen, Y. Yuan, J. Wang, Intercellular delivery of bioorthogonal chemical receptors for enhanced tumor targeting and penetration, Biomaterials 259 (2020), 120298.
[56] R. Wei, Y. Dong, Y. Tu, S. Luo, X. Pang, W. Zhang, W. Yao, W. Tang, H. Yang, X. Wei, X. Jiang, Y. Yuan, R. Yang, Bioorthogonal pretargeting strategy for anchoring activatable photosensitizers on plasma membranes for effective photodynamic therapy, ACS Appl. Mater. Interfaces 13 (12) (2021) 14004–14014.
[57] Y. Yuan, S. Xu, X. Cheng, X. Cai, B. Liu, Bioorthogonal turn-on probe based on aggregation-induced emission characteristics for cancer cell imaging and ablation, Angew. Chem. Int. Ed. Eng. 55 (22) (2016) 6457–6461.
[58] S.D. Huo, H.L. Ma, K.Y. Huang, J. Liu, T. Wei, S.B. Jin, J.C. Zhang, S.T. He, X. J. Liang, Superior penetration and retention behavior of 50 nm gold nanoparticles in tumors, Cancer Res. 73 (1) (2013) 319–330.
[59] K. Huang, H. Ma, J. Liu, S. Huo, A. Kumar, T. Wei, X. Zhang, S. Jin, Y. Gan, P. C. Wang, S. He, X. Zhang, X.J. Liang, Size-dependent localization and penetration of ultrasmall gold nanoparticles in cancer cells, multicellular spheroids, and tumors in vivo, ACS Nano 6 (5) (2012) 4483–4493.
[60] G. Mehta, A.Y. Hsiao, M. Ingram, G.D. Luker, S. Takayama, Opportunities and challenges for use of tumor spheroids as models to test drug delivery and efficacy, J. Control. Release 164 (2) (2012) 192–204.
[61] S. Daster, N. Amatruda, D. Calabrese, R. Ivanek, E. Turrini, R.A. Droeser, P. Zajac, C. Fimognari, G.C. Spagnoli, G. Iezzi, V. Mele, M.G. Muraro, Induction of hypoxia and necrosis in multicellular tumor spheroids is associated with resistance to chemotherapy treatment, Oncotarget 8 (1) (2017) 1725–1736.
[62] X. Huang, J. Zhuang, S.W. Chung, B. Huang, G. Halpert, K. Negron, X. Sun, J. Yang, Y. Oh, P.M. Hwang, J. Hanes, J.S. Suk, Hypoxia-tropic protein nanocages for modulation of tumor- and chemotherapy-associated hypoxia, ACS Nano 13 (1) (2019) 236–247.
[63] D. Khaitan, S. Chandna, M.B. Arya, B.S. Dwarakanath, Establishment and characterization of multicellular spheroids from a human glioma cell line; Implications for tumor therapy, J. Transl. Med. 4 (2006) 12.